

Probe assisted localized doping of aluminum into silicon substrates

Cite as: J. Appl. Phys. **125**, 075706 (2019); <https://doi.org/10.1063/1.5065385>

Submitted: 09 October 2018 . Accepted: 01 February 2019 . Published Online: 20 February 2019

Jung-Joon Ahn, Santiago D. Solares, Lin You, Hanaul Noh , Joseph Kopanski , and Yaw Obeng 



View Online



Export Citation



CrossMark

Ultra High Performance SDD Detectors



See all our XRF Solutions

Probe assisted localized doping of aluminum into silicon substrates

Cite as: J. Appl. Phys. 125, 075706 (2019); doi: 10.1063/1.5065385

Submitted: 9 October 2018 · Accepted: 1 February 2019 ·

Published Online: 20 February 2019



Jung-Joon Ahn,^{1,2,a)} Santiago D. Solares,^{2,b)} Lin You,¹ Hanaul Noh,²  Joseph Kopanski,^{1,c)}  and Yaw Obeng^{1,d)} 

AFFILIATIONS

¹Physical Measurement Laboratory, National Institute of Standards and Technology, Gaithersburg, Maryland 20899, USA

²Department of Mechanical and Aerospace Engineering, The George Washington University, Washington, DC 20052, USA

^{a)}Electronic addresses: ahn@gwu.edu and jna@nist.gov

^{b)}E-mail: ssolares@gwu.edu

^{c)}E-mail: joseph.kopanski@nist.gov

^{d)}E-mail: yaw.obeng@nist.gov

ABSTRACT

Precise control of dopant placement is crucial for the reproducible, and reliable, nanoscale semiconductor device fabrication. In this paper, we demonstrate an atomic force microscopy (AFM) probe assisted localized doping of aluminum into an n-type silicon (100) wafer to generate nanoscale counter-doped junctions within two nanometers of the silicon-air interface. The local doping results in changes in electrostatic potential, which are reported as contact potential difference, with nanoscale spatial resolution. In contrast to the literature where nano-mechanical defects in, or contaminants on, silicon substrates can result in measurable changes in the chemical potential of the near-surface, additional thermal treatment was needed to electrically activate the aluminum dopants in our current work. Unfortunately, the thermal activation step also caused the dopants to diffuse and geometric distortions in the doped area, i.e., broadening and blurring of the electrically distinct areas. The results from optimization efforts show that the “active” dopant concentration depended primarily on the thermal anneal temperature; additional AFM-tip dwell time during the aluminum implantation step had no meaningful impact on the electrical activity of the doped sites.

<https://doi.org/10.1063/1.5065385>

I. INTRODUCTION

In order to achieve reliable operation of nanoscale electronic devices, it is very important to precisely control the number and the placement of dopants in the semiconductor structure.^{1–3} The ability to implant small clusters of dopants with a precision of a few nanometers may also make it possible to engineer the barrier height in metal-semiconductor junctions.⁴ Due to the difficulties involved in realizing tightly controlled doping of nanoscale semiconductor structures, there has been increasing interest in new technologies that could enable the production of highly selective, uniform and ultra-shallow doped junctions at the channel regions in emerging nanoscale devices.^{5,6}

Atomic force microscopy (AFM) has been widely used as a nanoscale measurement tool.^{7–13} AFM-based nano-indentation has also been used as a fast and straightforward method to study the surface deformation,^{14–18} the nanoscale hardness, the

stiffness, and the elastic modulus of materials, with the aid of contact mechanics models of materials.^{19–22} Besides the metrological applications, AFM technology has also been used to manipulate the local physico-chemical properties of materials. For example, by indenting a semiconductor surface with an AFM tip, it is possible to modify the local surface morphology, as well as the physical and chemical characteristics at the nanoscale.^{23–26} However, the indentation performance of the AFM tip is highly dependent on factors such as the stiffness of the cantilever, the shape of the tip and the force applied by the tip.^{21–24} Homma *et al.* have shown that AFM nano-indentation can introduce nanoscale mechanical defects in silicon substrates and that such damage can result in changes in the near-surface chemical potential.²⁵ Similarly, Furukawa *et al.* have also shown that locally doped regions can be formed on a semiconductor by the physical placement of dopant atoms on the substrate's surface.²⁶

In this paper, we combine nano-indentation using AFM probe tip (with a loading force of ≈ 1 GPa) with an electrical voltage pulse to push dopant atoms into a substrate to create a locally doped region. The purpose of the voltage pulse is to enhance impurity introduction into the near-surface of the substrate. As a demonstration of this probe assisted doping (PAD) technique, we locally doped n-type silicon (Si) substrates with aluminum (Al) atoms, to within 2 nm of the substrate-air interface, with nanoscale spatial resolution. The resultant local electrostatic potential changes were measured with scanning Kelvin probe microscopy (SKPM) techniques and reported as contact potential difference (CPD). It must be noted that the contact potential differences reported in this work represent the relative difference between the contact potentials of the PAD processed areas and the pristine substrate; the CPD is not the absolute difference in electrochemical potentials of substrates. In contrast to Furukawa *et al.*, the as-introduced dopants had to be thermally activated to create electrically active nanoscale defects at the substrate's near-surface, even though we used the same loading force in the dopant placement. This PAD method is applicable to various dopants for which there are suitable precursors. For example, in probe-assisted P-doping, it should be possible to indent through an overcoat layer of highly doped phosphosilicate glass (PSG) film to introduce P-dopants into the underlying substrate.^{27,28}

While we have previously shown that doping concentrations can be estimated from the measured CPD,²⁹ the focus of this paper is to demonstrate the concepts of probe assisted localized doping of Si substrates. Special cross-calibrated Al-doped samples would be needed to provide quantitative dopant concentrations for this PAD demonstration. This work is in progress in our laboratory, hence, we do not discuss such quantitative dopant concentrations in this paper. However, based on our qualitative observations, we postulate that the exact concentration and distribution of dopants introduced into the substrate with this PAD technique will depend on several experimental parameters such as, but not limited to, precursor overcoat layer thickness, probe tip diameter, penetration depth, and thermal anneal temperature. These factors will need to be optimized to obtain the desired level of doping and lateral resolution for an intended application. As an application example, the electrically active implants can be organized into electrically readable identification markings for product authentication³⁰ and other emerging nano-electronic devices.

II. EXPERIMENTAL METHODS

A. Sample preparation

An n-type Si (100) substrate (1–10 Ω cm) was pre-cleaned using the standard RCA cleaning procedures,³¹ which include an initial surface organic cleaning step using SC-1 (5-parts H_2O :1-part NH_4OH :1-part H_2O_2), followed by an oxide stripping step using a HF solution (1-part HF mixed with 50 parts H_2O), a metallic ion removal step using SC-2 (5-parts H_2O :1-part HCl mixed with 1-part H_2O_2), and thoroughly rinsed with deionized

(DI) water, and finally blown dry with dry-nitrogen jet. After RCA cleaning, the substrate was processed in an electron beam (e-beam) evaporator to deposit an Al overcoat layer of ≈ 15 nm thickness. Al was used in the PAD demonstration because the material was readily available, and the overcoat layer was stable in air.

B. PAD mechanism and protocol

Figure 1 shows a schematic, and process flow, of the main concepts of the PAD technique presented in this paper. The PAD experiments were conducted using a Dimension 5000 and Nanoscope V AFM system (Bruker, CA) with a modified ramping mode as shown in Fig. 1(a) indenting through the Al overcoat layer in 3×3 indentation arrays of over a $1.5 \times 1.5 \mu\text{m}^2$ area, to a depth of 1.5 nm to 2 nm. The AFM tip loading force was about 1 GPa, i.e., $38.12 \mu\text{N}$, at the tip. The maximum AFM load was chosen to ensure that the tip traversed the entire Al overcoat layer to reach into the silicon substrate. The as-deposited Al dopants were electrically activated by thermal annealing using a RTA tool (600 $^\circ\text{C}$, 20 s, dry N_2 ambient, AS-Master, AnnealSys, Montpellier, France). The changes in the substrate's surface potential (CPD) were measured with SKPM, using a relatively sharp tip (<25 nm in tip radius) at a probe lift height of 5 nm.

Force-distance curves were used to understand penetration response of the AFM tip into the thin Al overcoat layer. The displacement of the tip along the Z-axis during indentation was obtained from the deflection of the cantilever (Δz , in units of distance), given in Eq. (1), where ΔV is the voltage increment in the photo-detector vertical signal as the tip is brought into contact with the sample, and S is the deflection-to-voltage sensitivity, measured through a force curve performed on a rigid sample (e.g., 100 nm of thermally grown SiO_2). For the diamond-coated tip used in the experiments, S is $\approx 63.64 \text{ nm/V}$

$$\Delta z = S \times \Delta V. \quad (1)$$

The tip load, p , for a general tip-sample contact can be expressed as

$$p = \Delta z \times k, \quad (2)$$

where the spring constant, k , is 58.53 N/m, as measured via the standard thermal noise calibration equation.³² The penetration depth, δ , due to p is defined as

$$\delta = Z - \Delta z, \quad (3)$$

where Z represents the piezo-scanner displacement along the axis perpendicular to the sample plane, toward the sample.

In these experiments, the maximum tip loading force, p_{max} , was determined from the deflection trigger thresholds, V_{TT} , which define the deflection limit of the cantilever

$$p_{\text{max}} = S \times V_{\text{TT}} \times k. \quad (4)$$

In order to traverse the entire thickness of the Al overcoat layer and to make sure that the tip contacts the Si surface, a V_{TT} of 9 V was required.

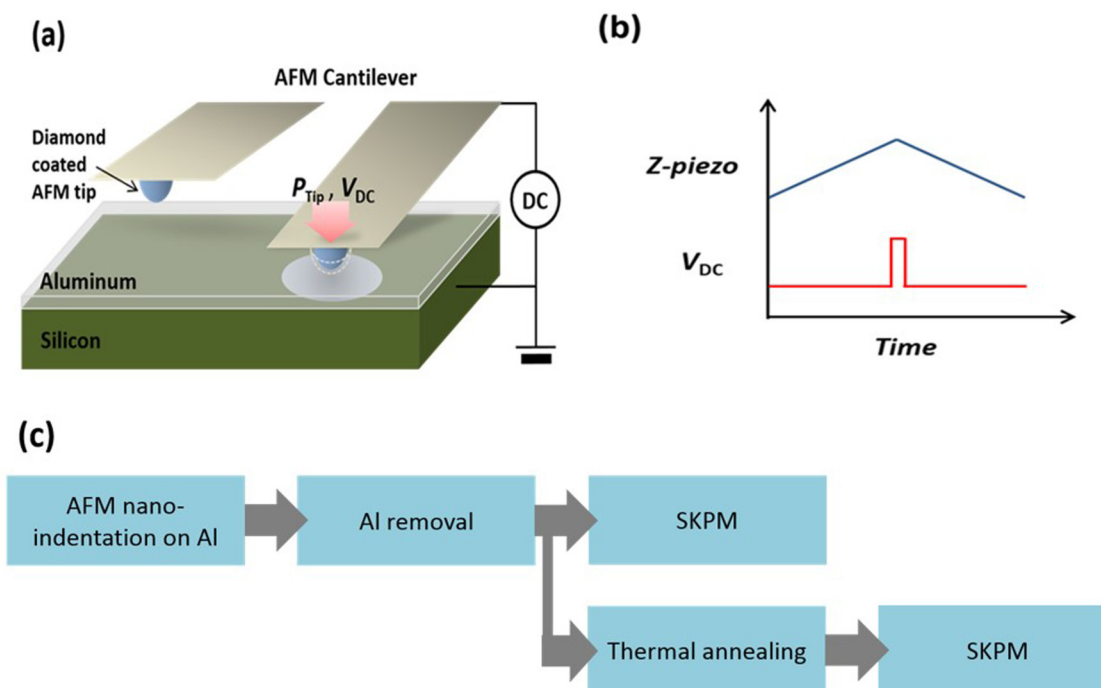


FIG. 1. Graphic illustration of the key concepts in the probe-assisted doping technique: (a) schematic of atomic force microscopy-based PAD of Al into an n-type Si (100) substrate. (b) A DC voltage pulse applied during the PAD process to enhance the interaction of the dopants with the Si substrate. (c) Block diagram of the experimental process flow.

To help the reader visualize the probe-assisted doping technique described in this paper, Fig. 1 shows a graphic illustration of the key concepts and the major process steps used in the technique. As mentioned above, in addition to the mechanical load on the AFM tip, we also applied a brief pulse of DC voltage when the AFM tip contacted the Al-Si interface, as shown in Fig. 1(b). This voltage pulse is meant to afford dopant insertion into the substrate along the lines of current-induced surface modification, where a voltage is applied to the probe tip to chemically activate the Si surface for the dopant placement.³³ In this PAD context, this voltage pulse presumably enhances amorphization/phase transition of Si under the AFM tip during the mechanical indentation.^{34–36} To accomplish this, we coupled the AFM to a pulse generator and synchronized the pulse of the DC voltage to the z-piezo scanner signal and synchronized the voltage pulse with the lowest position of the tip (i.e., at the maximum load force applied to the probe tip). Thus, no bias was applied to the tip while it was penetrating the Al overcoat layer; the DC voltage pulse was applied only when the tip reached the Si surface. The magnitude of the voltage applied to the AFM tip varied from -8 V to 8 V for various durations, of which the combination of 8 V for 20 ms provided the largest change in the surface potential (i.e., -21 mV). Applied pulse of less than 8 V resulted in the surface potential change of about 0.3 mV , which is difficult

to distinguish from the background surface potential. In addition, the AFM dwell time (i.e., how long the AFM tip remained in contact with the silicon substrate after the maximum applied load was applied) varied.

The thermal activation of the mechanically implanted Al dopants was studied by comparing the contact potential of RTA annealed samples to their analogous un-annealed samples, after the Al overcoat layer was removed by chemical wet etching using SC-2 and HF solutions. Subsequently, the dopant diffusion characteristics were investigated by measuring the changes in CPD as the RTA annealing temperature varied in the $500\text{ }^{\circ}\text{C}$ – $700\text{ }^{\circ}\text{C}$ range, while the AFM-tip dwell time also varied systematically from 0 to 3 s.

III. EXPERIMENTAL RESULTS

It is difficult to estimate the nano-indentation response of the thin metal films since it depends on numerous experimental factors such as the presence of an oxide layer, tip geometry, surface roughness, and thickness of the film, as well as crystal morphology within the film.^{21–23} Furthermore, there is no analytical model to estimate the indentation behavior when the penetration is close to the full thickness of the thin film where plastic deformation and rupture of the material are expected.²⁴ In order to understand the deformation response of Al overcoat layer and verify the type of

deformation at corresponding tip loading force, we measured the force–distance curves on Al overcoat layer and compared them with the predictions of Hertz contact model.¹⁷ While none of the numerous indentation models can fully characterize the indentation experiments described in this work, the Hertzian model is used for illustrative purposes only and out of convenience.

In an isotropic material, the predicted tip loading force for the Hertz contact model is given as

$$p_H = \frac{3}{4} E_{eff} \sqrt{R} \delta^{\frac{3}{2}}, \tag{5}$$

where E_{eff} is the effective value of Young’s modulus and R is the radius of curvature of the tip apex, approximately 185 nm in our case. E_{eff} can be obtained using the following relation:

$$\frac{1}{E_{eff}} = \frac{1 - \nu_{sample}^2}{E_{sample}} + \frac{1 - \nu_{tip}^2}{E_{tip}}, \tag{6}$$

where ν is the Poisson ratio and the sub-index “tip” corresponds to the mechanical properties of the AFM probe, while “sample” indicates the mechanical properties of Al overcoat layer and Si substrate together (Table 1).³⁷ We assumed that the Al overcoat layer and the substrate were in direct intimate contact. In applying the Hertz model, we used the modulus of Si and Al overcoat layer, namely, 130 GPa and 34.9 GPa, respectively.^{36,37} Due to the large Young’s modulus of our tip (≈ 750 GPa),³⁷ we did not consider any changes in tip radius caused by tip wear.

Figure 2 shows a typical variation of tip loading force in terms of the penetration depth, while we varied V_{TT} from 0 V to 9 V. The tip loading force-indentation response curves varied substantially from run to run, hence it would be meaningless to represent the data with a statistical representative plot. The variability in the loading force curves is probably from the thickness uniformity and rapture under load of the Al overcoat layer used. We also observed multiple step-like changes in the force–displacement curve for the Al overcoat layer, which are attributable to load induced thermo-mechanical property changes of the Al overcoat layer and at Al-Si interface.³⁷ The inset of Fig. 2 shows the comparison of the measured indentation curve on the Al overcoat layer to the expected Hertz contact response for an indentation up to 3 nm (the small indentation range was chosen to exclude the effect of the substrate on the indentation force). The measured force curves showed steeper slopes than for the Hertz

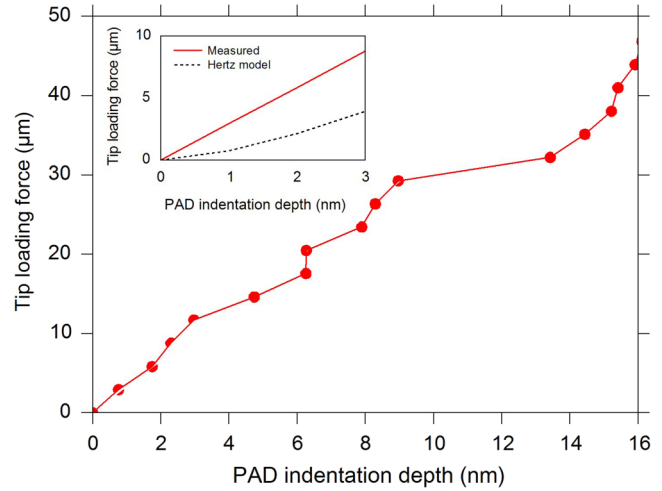


FIG. 2. A typical tip loading force-indentation response on the Al overcoat layer; the tip loading force-indentation response curves varied substantially from run to run, probably from the thickness reproducibility and uniformity of the Al overcoat layer used. The inset plot compares the measured force curve with the Hertz model based elastic response within for the first 3 nm of penetration.

contact model which suggests spontaneous rapture of the Al overcoat layer under test, long before showing any elastic response.

The electrical impact of the Al doping was evaluated by measuring changes in the local surface potential by SKPM techniques. SKPM measures the contact potential difference (CPD) between the tip and the sample at the nanoscale,^{38–42} which is defined as

$$V_{CPD} = \frac{1}{e} (\Phi_{tip} - \Phi_{sample}), \tag{7}$$

where e is the charge of the electron, Φ_{tip} and Φ_{sample} are the work functions of the AFM tip and sample, respectively. Here, a Platinum-Iridium (Pt/Ir) coated tip was used to measure the CPD, which is different from that used for the mechanical indentation (i.e., diamond coated tip).

An AC bias of 2 V in amplitude was applied to the tip to produce an electrostatic force on the cantilever, which is proportional to the CPD between the tip and the sample. The measurements were performed in two passes. The first scan was used to obtain the topography of the sample, and the second scan, during which the tip was not mechanically driven, was used to measure the CPD at a 5 nm lift offset above the sample surface. The samples were pre-cleaned with RCA cleaning before the SKPM measurement.

The “as-implanted” dopants were not electrically active and had to be thermally activated.^{43–45} However, thermal annealing techniques result in an unacceptable broadening of the junction profiles and an increase in the junction depth of the source/drain contacts.^{44,45} Of the available thermal annealing options, we elected to use RTA because it offers

TABLE I. Elastic constants for the materials and AFM tip used.³⁷ The Al properties are those for a thin film (<100 nm).

Sample	Young’s modulus (GPa)	Poisson’s ratio	Spring constant (N/m)
Si (100), N-type	130	0.18	...
Al	34.9	0.32	...
Diamond coated AFM tip	750	0	58.53

several potential advantages such as minimized dopant redistribution and required no capping.⁴⁵ Figure 3 presents the topography and CPD image of the PAD-processed Si surface after Al removal before [Figs. 3(a) and 3(b)] and after [Figs. 3(c) and 3(d)] the thermal annealing, respectively. The areas corresponding to the indents are marked with red dots in Figs. 3(b) and 3(d). In addition, the profile of the dashed line shown in Fig. 3 will be discussed in Fig. 4. The inspection of Fig. 3(b) reveals that the sample which was not annealed with RTA shows almost no change in CPD, even though there is obvious topographical variation due to the indents, as seen in Fig. 3(a). On the other hand, Fig. 3(d) shows changes in surface CPD after the RTA anneal. After the RTA process, the CPD changed by about $-29 \text{ mV} \pm 6 \text{ mV}$ over the PAD processed area, as shown in Fig. 3(d). The white streaks in Figs. 3(a) and 3(c) are probably due to pile-up from the indentation process based on their CPD values, which are consistent with the Si substrate as shown in Figs. 3(b) and 3(d).

Figure 4 compares the combined CPD and AFM topography indent line profiles for (a) PAD doped sites before (a) and after (b) RTA treatment, which correspond to the dashed lines shown in Fig. 3. Close inspection of the micrographs reveals that the CPD area is larger for thermally annealed samples than that of the un-annealed samples. Furthermore, the CPD image seems blurred along the perimeter for the annealed samples, probably due to the diffusion of the Al-dopants, although there could be other mechanistic explanations for this observation.

In an effort to further understand the diffusion of activated Al dopants during the thermal anneal, the combined effect of the AFM-probe dwell time and the annealing temperature were investigated. The sample processed with RTA at 500°C , the CPD varied in the -21 mV to -32 mV range, while the CPD ranged from -36 mV to -51 mV on the samples processed at 600°C . In addition, the size of the electrically active area increased by over 40% when the annealing

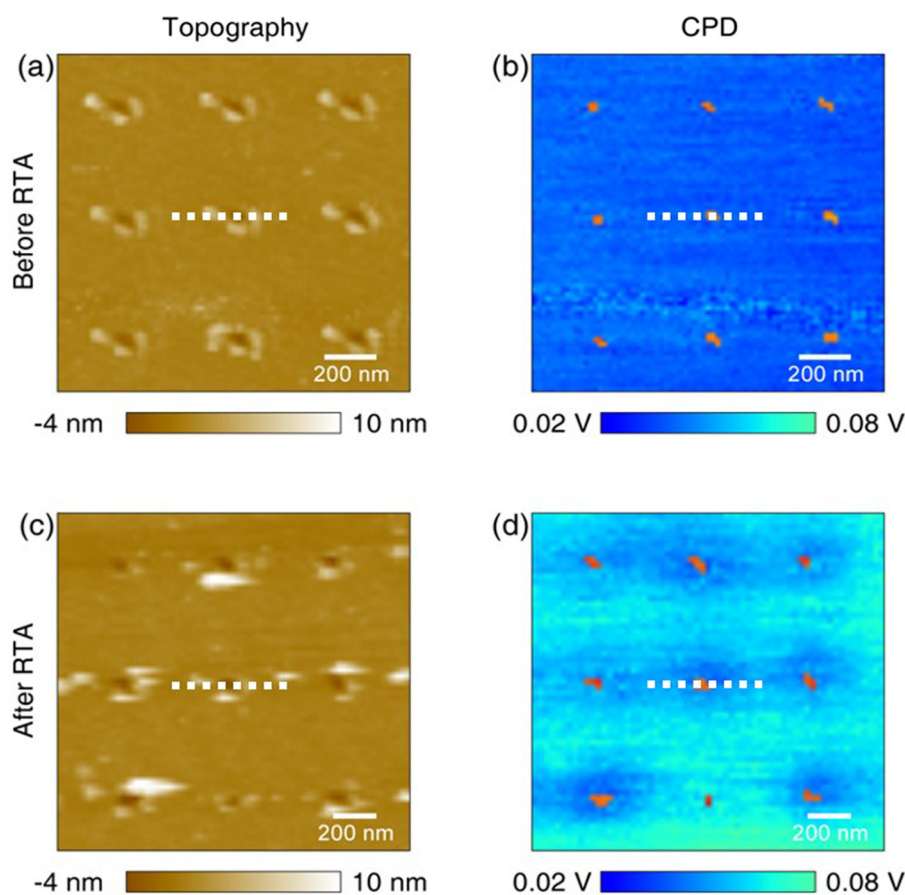


FIG. 3. (a) AFM topography of 3×3 arrays of PAD processed n-type Si (100) surface without RTA and (b) corresponding CPD image of the same area. The red colored areas were manually added to indicate the indent sites with a depth profile $>1.5 \text{ nm}$. (c) 3×3 arrays of PAD processed n-type Si (100) surface with RTA performed after removing the Al overcoat layer and (d) corresponding CPD image of the same area. The red colored areas were manually added to indicate the indent sites with a depth profile $>1.5 \text{ nm}$.

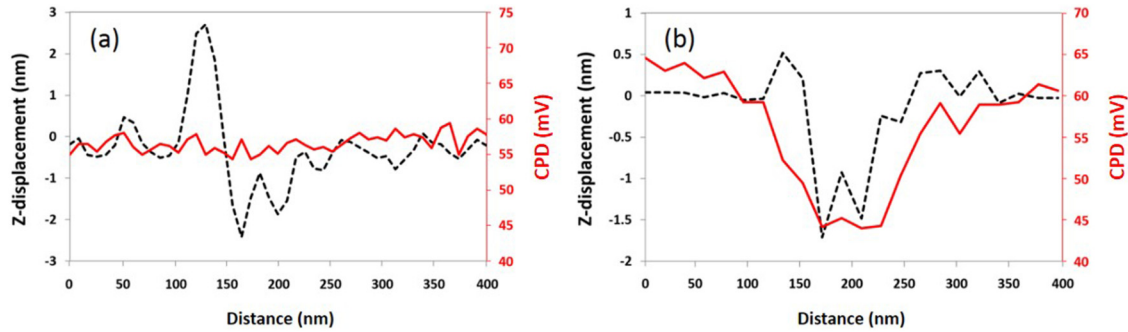


FIG. 4. Comparison of the topography and CPD line profile: (a) AFM topography and CPD line profiles from an indentation of PAD processed n-type Si (100) surface before RTA and (b) corresponding topography and CPD profile of the same area after RTA. The AFM topography and CPD line profile in Figs. 4(a) and 4(b) correspond to dashed lines in Figs. 3(a) and 3(c) and 3(b) and 3(d), accordingly.

temperature was increased from 500 °C to 600 °C and by over 70% when the temperature was further increased to 700 °C. Since there was no further injection of aluminum by PAD after RTA, these observations suggest that both the number of electrically active dopants, and the diffusion range of the Al dopants in the silicon increased with increasing RTA process temperature. These observations suggest that (i) CPD is a reasonable metric for monitoring the electrical response of the sub-surface doping, (ii) some thermal treatment was needed to thermally activate the dopants, and lower the energy level at the Si surface due to an increased concentration of holes,⁴⁶ and (iii) the implanted Al dopants out-diffused from the point of introduction with the thermal anneal.

The RTA temperature and AFM dwell time ranges were explored in an attempt to fully optimize the thermal anneal process for maximum dopant activation. The maximum CPD values in PAD processed area were compared in terms of annealing temperature and tip dwell times as shown in Fig. 5.

The data in Fig. 5 clearly shows that the “active” dopant concentration depended on both the RTA temperature and the AFM tip dwell time. That the CPD data converge at 700 °C can be attributed to possible dopant loss due to evaporation during high temperature anneal, as shown by Murarka,⁴⁷ and/or to volumetric dilution of the activated dopants as the Al diffuses further away from the PAD site at higher temperatures. Furthermore, the data suggest that at 700 °C, the CPD was independent of the probe tip dwell time during the indentation step. In fact, statistical analyses of the CPD data, not presented in this paper for brevity, indicate that the additional dwell time had no meaningful impact on the doping process and the resultant electrical activity of the doped sites.

IV. DISCUSSION

Mechanistically, it is reasonable to describe the observed change in CPD as a function of the local chemical potential shown as follows:

$$V_{CPD} = F[\mu(p, T, C)], \quad (8)$$

$$V_{CPD(AI-PADD)} = V_{SP}^0 + \Delta V_{SP}^{NI} + \Delta V_{SP}^{doping} + \Delta V_{SP}^{TT}. \quad (9)$$

In solid systems, the chemical potential can be changed by applying external stimuli (high temperature, pressure, local chemistry changes by localized doping, etc.), which affect the phase of the material and the electronic structure.^{25,34} The CPD values [from Eq. (7)] represent the difference between the surface potential of the sample and that of the tip. As described by Eq. (9), the surface potential of the PAD Al-doped sites is different from that of the pristine Si surface. The new surface potential depends on many variables, such as native oxides (V_{SP}^0), nano-indentation (ΔV_{SP}^{NI}), doping (ΔV_{SP}^{doping}), and thermal treatment (ΔV_{SP}^{TT}), which together determine the chemical potential of the modified surface. Any further processing, such as

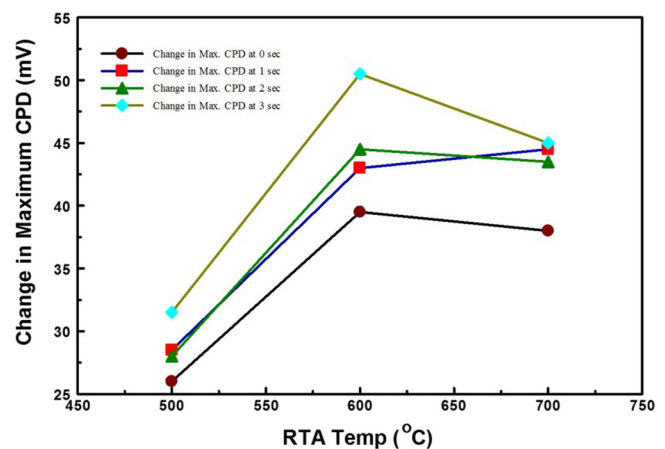


FIG. 5. Plot of the calculated changes in the maximum CPD values at the PAD sites as a function of the nominal RTA annealing temperature and AFM-tip dwell time. The data points represent the results of the calculation and hence has no error bars. The connecting lines between the individual points are just a visual aid.

thermal annealing causes further shifts in this new surface potential.

V. CONCLUSION AND OUTLOOK

In this work, we have demonstrated an AFM-based probe-assisted local doping technique and successfully illustrated it with Al doping of an n-type Si substrate. The tip-force load curves show that the probe-assisted implantation of the dopant is complicated at the indentation stage by experimental artifacts such as dopant film inhomogeneity and premature load induced film rapture. Nevertheless, the doping resulted in modifications in local electrical characteristics, reported as changes in CPD. In stark contrast to the previous results in the open literature, our data indicate that a thermal step is needed to make the dopants electrically active. Qualitatively, the number of activated dopants increased with increasing activation temperature. The thermal activation results in undesired diffusion of the dopants away from their intended location, leading to resolution loss. However, the electrical results indicate that the electrical activation and the diffusion of Al dopants can be controlled and must be optimized to balance the electrical performance and the resolution of the junctions created by the probe assisted implantation in the intended application.

As the semiconductor industry continues to produce ever smaller devices, new fabrication and metrology techniques are needed. The ultimate sizes and functionality of these new emerging devices will be determined by fundamental and engineering limits. Currently, traditional metrology cannot adequately address the emerging metrology needs.⁴⁸ The PAD technique and the SKPM-based junction metrology described in this paper are viable contributions to this quest.

ACKNOWLEDGMENTS

This is a contribution of the National Institute of Standards and Technology, not subject to copyright.

Certain commercial equipment, instruments, or materials are identified in this report paper to specify the experimental procedure adequately. Such identification is not intended to imply recommendation or endorsement by the National Institute of Standards and Technology or the United States Government Publishing Office, nor is it intended to imply that the materials or equipment identified are necessarily the best available for the purpose.

REFERENCES

- ¹M. Hori, T. Shinada, Y. Ono, A. Komatsubara, K. Kumanogi, T. Tani, T. Endoh, and I. Ohdomari, *Appl. Phys. Lett.* **99**, 062103 (2011).
- ²M. Fuechsle, J. A. Miwa, S. Mahapatra, H. Ryu, S. Lee, O. Warschkow, L. C. L. Hollenberg, G. Klimeck, and M. Y. Simmons, *Nat. Nanotechnol.* **7**, 242 (2012).
- ³Y. Taur, H. P. Chen, W. Wang, S. H. Lo, and C. Wann, *IEEE Trans. Electron Dev.* **59**, 863–866 (2012).
- ⁴M.-S. Kang, J.-J. Ahn, K.-S. Moon, and S.-M. Koo, *Nanoscale Res. Lett.* **7**, 75 (2012).
- ⁵T. Shinada, S. Okamoto, T. Kobayashi, and I. Ohdomari, *Nature* **437**, 1128 (2005).
- ⁶H. Kambayashi, Y. Nuuyama, S. Ootomo, T. Nomura, M. Iwami, Y. Satoh, S. Kato, and S. Yoshida, *IEEE Electron Dev. Lett.* **28**, 1077–1079 (2007).
- ⁷F. J. Giessibl, *Rev. Mod. Phys.* **75**, 949–983 (2003).
- ⁸R. Garcí'a and R. Pérez, *Surf. Sci. Rep.* **47**, 197–301 (2002).
- ⁹L. Gross, F. Mohn, N. Moll, P. Liljeroth, and G. Meyer, *Science* **325**, 1110 (2009).
- ¹⁰P. Avouris, T. Hertel, and R. Martel, *Appl. Phys. Lett.* **71**, 285–287 (1997).
- ¹¹J.-J. Ahn, Y.-D. Jo, S.-C. Kim, J.-H. Lee, and S.-M. Koo, *Nanoscale Res. Lett.* **6**, 235 (2011).
- ¹²J. J. Kopanski, L. You, J. J. Ahn, E. Hitz, and Y. S. Obeng, *ECS Trans.* **61**, 185–193 (2014).
- ¹³L. You, J.-J. Ahn, Y. S. Obeng, and J. J. Kopanski, *J. Phys. D Appl. Phys.* **49**, 045502 (2016).
- ¹⁴B. Bhushan and V. N. Koinkar, *Appl. Phys. Lett.* **64**, 1653–1655 (1994).
- ¹⁵M. R. Vanlandingham, S. H. Mcknight, G. R. Palmese, R. F. Eduljee, J. W. Gillespie, and J. R. L. Mcculough, *J. Mater. Sci. Lett.* **16**, 117–119 (1997).
- ¹⁶G. M. Pharr, *Mater. Sci. Eng. A* **253**, 151–159 (1998).
- ¹⁷E. G. Herbert, G. M. Pharr, W. C. Oliver, B. N. Lucas, and J. L. Hay, *Thin Solid Films* **398–399**, 331–335 (2001).
- ¹⁸Y. Cao, S. Allameh, D. Nankivil, S. Sethiaraj, T. Otiti, and W. Soboyejo, *Mater. Sci. Eng. A* **427**, 232–240 (2006).
- ¹⁹M. A. Monclus, T. J. Young, and D. Di Maio, *J. Mater. Sci.* **45**, 3190–3197 (2010).
- ²⁰J. J. Roa, G. Oncins, F. T. Dias, V. N. Vieira, J. Schaf, and M. Segarra, *Physica C Supercond.* **471**, 544–548 (2011).
- ²¹C. L. Kelchner, S. J. Plimpton, and J. C. Hamilton, *Phys. Rev. B* **58**, 11085–11088 (1998).
- ²²A. Bolshakov and G. M. Pharr, *J. Mater. Res.* **13**, 1049–1058 (1998).
- ²³D. E. Kramer, A. A. Volinsky, N. R. Moody, and W. W. Gerberich, *J. Mater. Res.* **16**, 3150–3157 (2001).
- ²⁴W. W. Gerberich, D. E. Kramer, N. I. Tymiak, A. A. Volinsky, D. F. Bahr, and M. D. Kriese, *Acta Mater.* **47**, 4115–4123 (1999).
- ²⁵T. Homma, M. Kato, N. Kubo, K. Sakata, and M. Yanagisawa, *J. Electrochem. Soc.* **156**, H475–H478 (2009).
- ²⁶T. Furukawa, J. J. Ellis-Monaghan, and J. A. Slinkman, U.S. patent 6,251,755 (26 June 2001).
- ²⁷D. Kobor, R. Ndioukane, O. Palais, M. Touré, A. K. Diallo, N. C. Y. Fall, and M. Biagui, *Appl. Phys. Res.* **7**, 8 (2015).
- ²⁸S. Werner, S. Mourad, W. Hasan, and A. Wolf, *Energy Proc.* **124**, 455–463 (2017).
- ²⁹S.-E. Park, N. V. Nguyen, J. J. Kopanski, J. S. Suehle, and E. M. Vogel, *J. Vac. Sci. Technol.* **24**, 404–407 (2006).
- ³⁰Y. S. Obeng, J. J. Kopanski, and J.-J. Ahn, U.S. patent 10,152,666 (1 December 2018).
- ³¹W. Kern, *J. Electrochem. Soc.* **137**, 1887–1892 (1990).
- ³²H. J. Butt and M. Jaschke, *Nanotechnology* **6**, 1 (1995).
- ³³T. C. G. Reusch, O. Warschkow, M. W. Radny, P. V. Smith, N. A. Marks, N. J. Curson, D. R. McKenzie, and M. Y. Simmons, *Surf. Sci.* **601**, 4036–4040 (2007).
- ³⁴I. Zarudi, W. C. D. Cheong, J. Zou, and L. C. Zhang, *Nanotechnology* **15**, 104 (2004).
- ³⁵W. B. Holzapfel and N. S. Issacs, *High pressure techniques in chemistry and physics—A Practical Approach* (Oxford University Press, 1997).
- ³⁶B. Lee, S. Lee, H. Lee, and H. Shin, *Proc. SPIE* **4557**, 8 (2001).
- ³⁷W. D. Nix, *Metall. Mater. Trans. A* **20**, 2217 (1989).
- ³⁸M. Nonnenmacher, M. P. O'Boyle, and H. K. Wickramasinghe, *Appl. Phys. Lett.* **58**, 2921–2923 (1991).
- ³⁹A. Kikukawa, S. Hosaka, and R. Imura, *Appl. Phys. Lett.* **66**, 3510–3512 (1995).
- ⁴⁰S. I. Kitamura and M. Iwatsuki, *Appl. Phys. Lett.* **72**, 3154–3156 (1998).
- ⁴¹D. Ziegler and A. Stemmer, *Nanotechnology* **22**, 075501 (2011).
- ⁴²D. Ziegler, P. Gava, J. Guttinger, F. Molitor, L. Wirtz, M. Lazzeri, A. M. Saitta, A. Stemmer, F. Mauri, and C. Stampfer, *Phys. Rev. B* **83**, 235434 (2011).

⁴³S. M. Hu, P. Fahey, and R. W. Dutton, *J. Appl. Phys.* **54**, 6912–6922 (1983).

⁴⁴J. R. Troxell, A. P. Chatterjee, G. D. Watkins, and L. C. Kimerling, *Phys. Rev. B* **19**, 5336–5348 (1979).

⁴⁵F. Lanzerath, D. Buca, H. Trinkaus, M. Goryll, S. Mantl, J. Knoch, U. Breuer, W. Skorupa, and B. Ghyselen, *J. Appl. Phys.* **104**, 044908 (2008).

⁴⁶T. Itoh, T. Inada, and K. Kanekawa, *Appl. Phys. Lett.* **12**, 244–246 (1968).

⁴⁷S. P. Murarka, *J. Appl. Phys.* **56**, 2225–2230 (1984).

⁴⁸N. G. Orji, M. Badaroglu, B. M. Barnes, C. Beitia, B. D. Bunday, U. Celano, R. J. Kline, M. Neisser, Y. Obeng, and A. E. Vladar, *Nat. Electron.* **1**, 532–547 (2018).